GEOLOGY

Geological records of transient fluid drainage into the shallow mantle wedge

Kazuki Yoshida[1]*, Ryosuke Oyanagi[2,3], Masao Kimura[4], Oliver Plümper[5], Mayuko Fukuyama[6], Atsushi Okamoto[1]*

Pore fluid pressure on subduction zone megathrusts is lowered by fluid drainage into the overlying plate, affecting subduction zone seismicity. However, the spatial and temporal scales of fluid flow through suprasubduction zones are poorly understood. We constrain the duration and velocity of fluid flow through a shallow mantle wedge based on the analyses of vein networks consisting of high-temperature serpentine in hydrated ultramafic rocks from the Oman ophiolite. On the basis of a diffusion model and the time-integrated fluid flux, we show that the channelized fluid flow was short-lived (2.1×10^{-1} to 1.1×10^{1} years) and had a high fluid velocity (2.7×10^{-3} to 4.9×10^{-2} meters second^{-1}), which is close to the propagation velocities of seismic events in present-day subduction zones. Our results suggest that the drainage of fluid into the overlying plate occurs as episodic pulses, which may influence the recurrence of megathrust earthquakes.

INTRODUCTION

Subduction zone seismicity is controlled by the pore fluid pressure on the plate interface (*1*–*3*). Accumulation of aqueous fluids generated by the decomposition of hydrous minerals in the subducting slab leads to a high pore fluid pressure (*4*). Such fluids move upward along the plate boundary megathrust (*5*, *6*) or migrate into the mantle wedge or lower crust of the overlying plate to cause partial melting or hydration (*7*, *8*). Recently, fluid drainage from the subducting slab into the mantle wedge and arc crust has been identified, based on increases in the ratio of *P*- and *S*-wave velocities (V_p/V_s) above the plate boundary (*9*), upward migration of seismicity into the overlying plate (*10*, *11*), and along-strike tremor migration (*12*). This fluid drainage may change the pore fluid pressure at the plate boundary and may control the recurrence of earthquakes (EQs) (*10*, *13*, *14*).

Channelized fluid flow on subduction zone interfaces is geologically recorded as mineral-filled fractures (i.e., veins), hydration and/or dehydration of ancient accretionary complexes, or exhumed metamorphic rocks (*15*, *16*). For example, the mantle wedge corner in subduction zones is thought to be intensively hydrated (i.e., serpentinized) or has experienced metasomatic reactions (*7*, *17*). Hydration of the mantle wedge reduces the pore fluid pressure, but once it is completely hydrated, a continuous supply of fluids causes an increase in fluid pressure, resulting in fracture propagation and migration of seismicity into the mantle wedge (*10*). However, it is challenging to constrain the time scales of short-term fluid flow events using conventional geochronological methods.

Infiltration of external fluid into fractures would induce formation of reaction zone along fracture wall of the host rocks. Several studies have investigated the widths and elemental profiles of these reaction zones along veins, revealing that the time scales of fluid-rock interactions in subducting oceanic crust (*18*) and middle continental crust (*19*) can occur over short time intervals (10^{-3} to 10^{2} years) compared with the entire duration of regional metamorphism (10^{5} to 10^{7} years). However, there have been no studies that provide geological constraints on the time scales and the velocities of fluid flow in the mantle wedge due to the rare occurrences of the geological structures that capture the time scales of fluid-rock interaction. The Oman ophiolite is one of the best-exposed ophiolites worldwide and contains a complete section from the crust to the uppermost mantle of the oceanic lithosphere. After its formation at the mid-ocean ridge, the Oman ophiolite was thrust over oceanic crust and sediments (*20*). Geochemical studies have revealed that fluids derived from the subducting slab were introduced into the mantle section of the Oman ophiolite (*21*, *22*). Therefore, the ophiolite provides an excellent opportunity to investigate fluid flow and fluid-rock interactions within the shallow mantle wedge.

In this study, we report the occurrence of an antigorite-chrysotile vein network developed in hydrated ultramafic rocks in the Oman ophiolite. The antigorite-chrysotile veins have a distinct reaction zone that consists of brucite (Brc). On the basis of detailed microstructural observations and trace element analysis, we constrained the timing and formation conditions of the antigorite-chrysotile veins. Mass balance and mineral-fluid equilibria calculations, coupled with a diffusion model for the reaction zone, allowed us to estimate the duration of vein formation and fluid flow velocity through the fractures. We then compared the fluid drainage characteristics through the shallow mantle wedge with characteristic velocities of propagation of seismic events obtained by geophysical observations in active subduction zones.

Oman ophiolite and CM1A site

The Oman ophiolite consists of an ~8-km-thick section of pillow lavas, a sheeted diabase dike complex, noncumulate gabbros, and cumulate gabbros, which are underlain by a 9- to 12-km-thick

[1]Department of Environmental Studies for Advanced Society, Graduate School of Environmental Studies, Tohoku University, 6-6-20 Aramaki-Aoba, Aoba, Sendai, Japan. [2]School of Science and Engineering, Kokushikan University, Tokyo 154-8515, Japan. [3]Research Institute for Marine Geodynamics, Japan Agency for Marine-Earth Science and Technology (JAMSTEC), Yokosuka 237-0061, Japan. [4]Institute of Materials Structure Science, High Energy Accelerator Research Organization (KEK), Tsukuba, Ibaraki 305-0801, Japan. [5]Department of Earth Sciences, Utrecht University, 3584 CD, Utrecht, Netherlands. [6]Graduate School of Engineering Science, Akita University, Akita 010-8502, Japan.
*Corresponding author. Email: kazuki.yoshida.t4@dc.tohoku.ac.jp (K.Y.); atsushi.okamoto.d4@tohoku.ac.jp (A.O.)

section of peridotite (*23*). These rocks formed at a fast-spreading ridge obducted over another section of oceanic crust and emplaced onto the Arabian Peninsula during the closure of the Tethys Ocean (*24*, *25*). The ophiolite records high-temperature alteration near the spreading center (*26*), off-axis low-temperature alteration on the seafloor (*27*, *28*), subduction-related high-temperature metamorphism (*20*, *29*, *30*), listvenite formation at ~90°C at the base of the mantle section (*31*), and present-day low-temperature (<50°C) serpentinization (*28*, *32*). The mantle section of the Oman ophiolite is moderate to highly (30 to 70%) serpentinized, which occurred on the seafloor at temperatures of 200° to 250°C (*27*, *28*) and on land at temperatures of <50°C (*28*, *32*).

We analyzed core samples of dunite recovered by the Oman Drilling Project (OmanDP; www.omandrilling.ac.uk) at Hole CM1A, located in the Wadi Tayin massif, Oman (22°54.435′N, 58°20.149′E; Fig. 1, A and B) (*33*). Hole CM1A penetrated the lower crust section (0 to 160 m depth), crust-mantle transition zone (160 to 310 m depth), and upper mantle section (310 to 404 m depth), and these three sections consist mainly of variably altered gabbroic rocks (olivine gabbro and troctolite; 5 to 95% altered), completely serpentinized dunites, and 70 to 100% serpentinized harzburgite, respectively (Fig. 1C) (*33*–*37*). These lithological sequences overlie the metamorphic soles (Fig. 1B), which may represent an ancient subduction zone setting (*20*, *30*).

RESULTS

Antigorite-chrysotile vein networks in serpentinized dunite

In the core from Hole CM1A, Atg-Ctl veins are present in dunite at the crust-mantle transition zone (160 to 180 m depth) and in some thin dunite layers in the upper mantle section (Fig. 2A). Figure 2 (B and C) shows x-ray computed tomography (CT) images and transmitted light thin-section scans of typical serpentinized dunite samples from the crust-mantle transition zone [samples C5707A-90Z-2 WW 48.0–53.0 (90Z2) and C5707A-137Z-3 WW 46.0–54.0 (137Z3)]. The serpentinized dunite samples consist of lizardite (Lz), Brc, magnetite (Mag), and relics of Cr-rich spinel. The samples have a mesh texture that was developed during serpentinization. Olivine and pyroxenes were not observed. Some dunite samples have undergone intense weathering (i.e., formation of coalingite, oxyhydroxides, and clays (Fig. 2C) (*33*). The distinct vein networks are characterized by high x-ray absorption (i.e., "bright veins") as compared with the matrix with a mesh texture (Fig. 2B and fig. S1A), whereas there is little contrast in the CT images of samples from depths near the mantle section (Fig. 2C and fig. S1B). The x-ray CT of the core sample shows extensive vein network and several cross-cutting relationships among the veins (fig. S2, A to D). A comparison of the x-ray CT images, microscopic observations, and identification of the serpentine based on Raman spectra (fig. S3) of thin sections revealed that the bright veins consist of antigorite (Atg) + chrysotile (Ctl) (referred to as "Atg-Ctl veins" hereafter). Along the veins, brucite-rich reaction zones spread into the wall rock from the vein walls (Fig. 2B and fig. S1A). These brucite-rich reaction zones are characterized by a Si-poor region (Si elemental

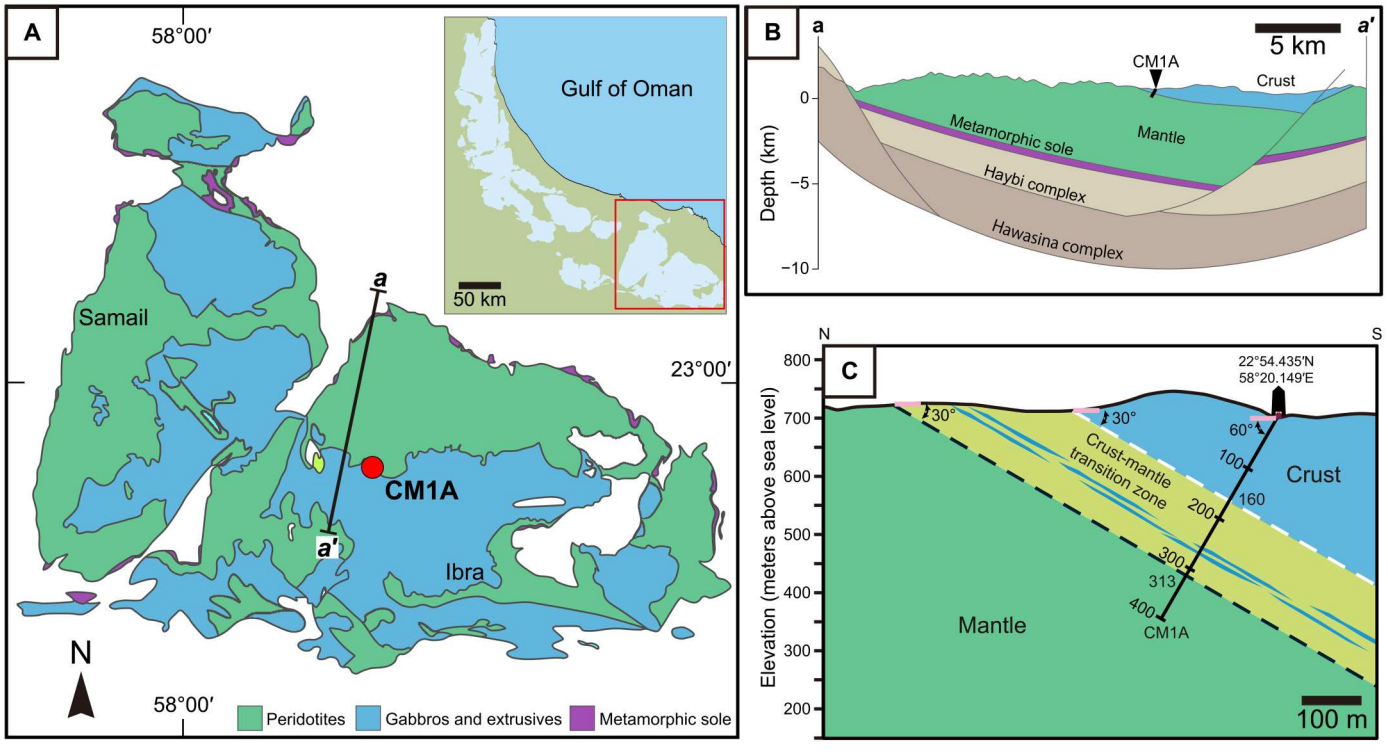

Fig. 1. Geological map of the drilling site CM1A borehole. (**A**) Geological map of the Wadi Tayin massif [following Nicolas *et al*. (*25*)]. The red circle marks the location of the drill site. (**B**)The cross section of *a*-*a*′ in (A) [following Searle (*30*)]. (**C**) Close-up of the cross section of the drill site [following Kelemen *et al*. (*33*)].

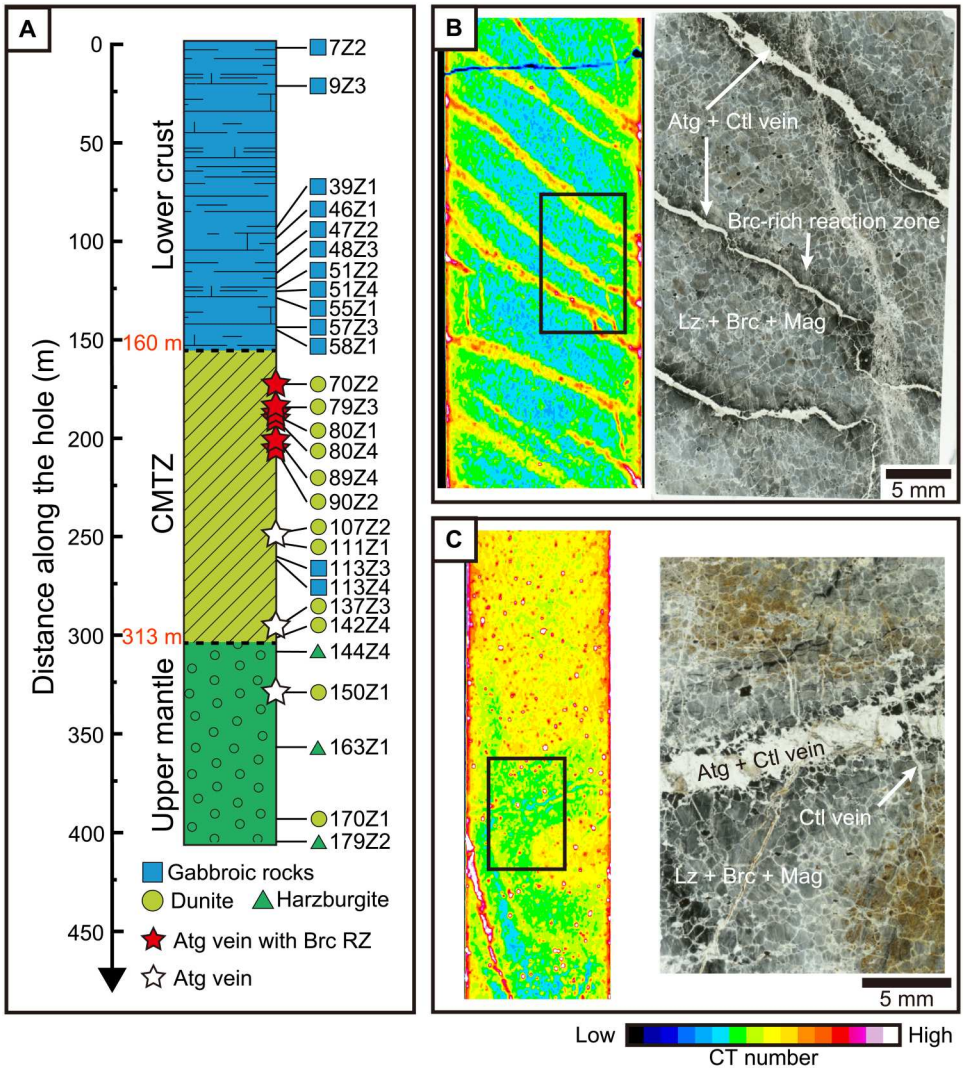

Fig. 2. Sample locations and descriptions along the drill core CM1A. (**A**) Location of the Atg-Ctl vein networks with and without Brc-rich reaction zones (RZs) are represented by red and white stars, respectively. CMTZ, crust-mantle transition zone. (**B** to **E**) Onboard x-ray computed tomography (CT) images and thin-section scans of samples (B) C5707A-90Z-2 WW 48.0–53.0 (90Z2) and (C) C5707A-137Z-3 WW 46.0–54.0 (137Z3), along with thin-section images. The regions represented by the black rectangles on the x-ray CT images were made into thin sections. The reaction zone in (B) has high x-ray absorption as compared with the matrix (Lz + Brc + Mag).

map; Fig. 3A). The orientations of the Atg-Ctl veins vary with borehole depth, and they are cut by late-stage Ctl veins (Fig. 2C) (*33*).

Microstructures and chemical characteristics of the Atg-Ctl veins and Brc-rich reaction zones

The microstructure and chemical composition were analyzed in detail for a typical Atg-Ctl vein in the dunite sample 90Z2 (Fig. 3A). Within the Atg-Ctl veins, bladed Atg (X_{Mg} = 0.97 to 0.98) 10 to 100 μm in length is randomly oriented (fig. S4, A and B), and fine-grained Ctl (X_{Mg} = 0.97 to 0.98) fills the space between Atg grains (fig. S5A). The dunite matrix consists of lizardite {97.5 area percent; X_{Mg} [Mg/(Mg + Fe)] = 0.97}, Brc (0.5 area percent; X_{Mg} = 0.85), and magnetite (2.0 area percent; 1 to 2 μm in size; fig. S5B), which is cut by Atg-Ctl veins with Brc-rich reaction zones (Fig. 3A).

The reaction zone consists of Brc (41.0 area percent; X_{Mg} = 0.88), Ctl (55.3 area percent; X_{Mg} = 0.97), and Mag (3.0 area percent; 1 to 2 μm in size; fig. S5C). In the reaction zone, Brc preferentially occurs in the mesh cores, and mesh rims are replaced by Ctl (Fig. 3B). Spontaneous channeling structures that are called wormholes (*38*, *39*) developed in the Brc-rich reaction zones (Fig. 3C), which propagate outwards from the boundaries with the Atg-Ctl veins (fig. S6, A to C). The wormholes are apparent through a magnetite coating at their boundaries to the matrix serpentinite (fig. S6C). The inside of the wormholes is filled with Ctl (X_{Mg} = 0.96 to 0.97). The reaction zone has a sharp boundary with the matrix on the millimeter- (Fig. 3A) to nanometer-scale (Fig. 3D) but preserves a mesh texture (Fig. 3A). Transmission electron microscopy (TEM) observations reveal Ctl in the spaces between Brc crystals in the reaction zone, and pores occur around Brc grains in the matrix (Fig. 3D and fig. S7, A and B). The width of the Brc-rich reaction zones ranges

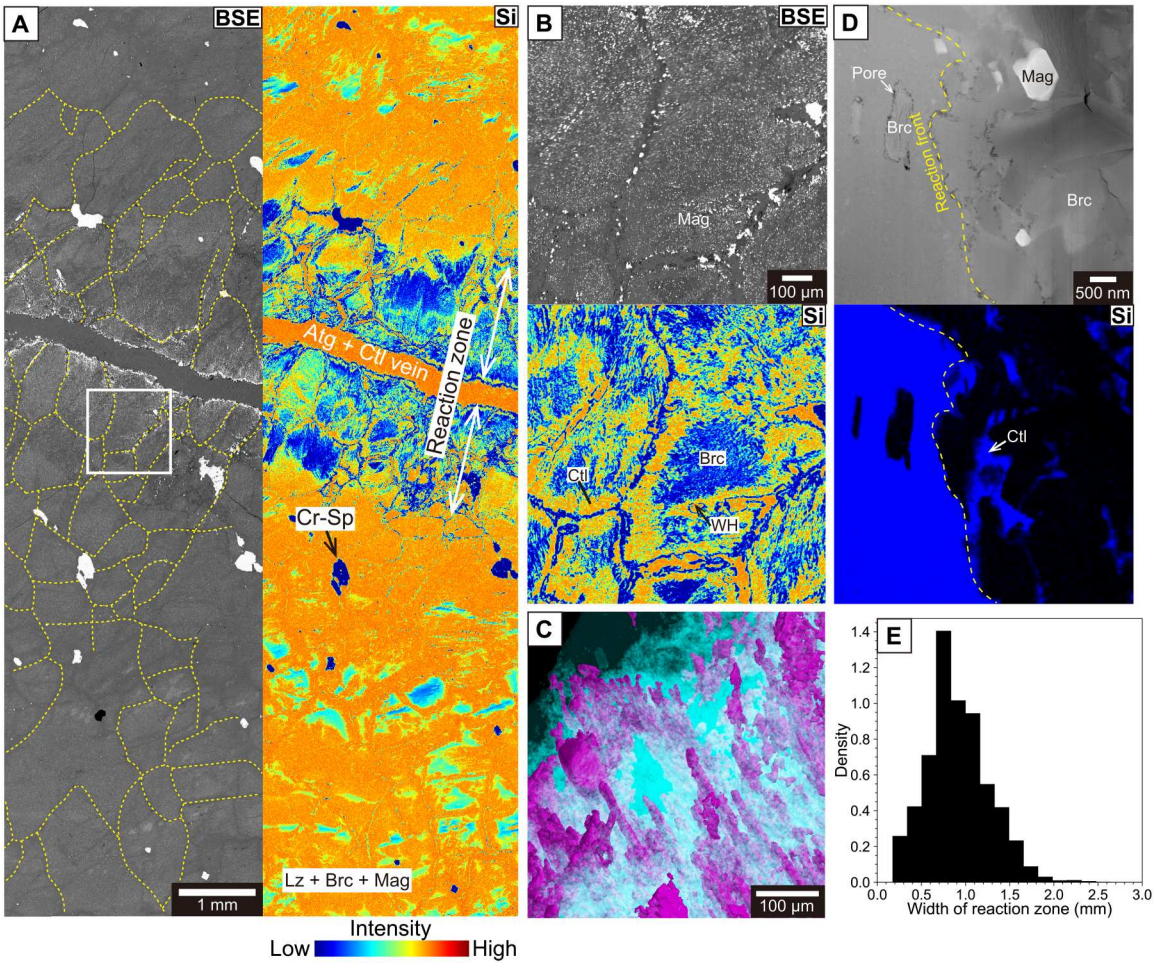

Fig. 3. Microstructure of the reaction zone and Atg-Ctl vein in a dunite sample (90Z2). (**A**) Back-scattered electron (BSE) image and Si elemental map of the brucite-rich reaction zone. The yellow dashed lines represent the boundaries of mesh domains. (**B**) BSE image and Si elemental map of the region indicated by the white box in (A). The reaction zone has a Brc mesh core and Ctl mesh rim. (**C**) High-resolution x-ray CT image of the reaction zone showing a three-dimensional wormhole (WH) structure that consists of magnetite (purple) and Brc (blue). The diameter of the wormhole is about 60 μm and is connected to the Atg vein (see also fig. S6). The distance between each wormhole is about 100 μm. (**D**) TEM image and energy-dispersive x-ray Si-map at the boundary between the reaction zone and matrix shows sharp reaction front. (**E**) Histogram of reaction zone widths for sample 90Z2.

from 0.5 to 1.3 mm (average = 0.88 mm; Fig. 3E) and is independent of the distribution of wormholes.

In situ trace element concentrations of the Atg-Ctl veins and lizardite in the matrix were analyzed by laser ablation inductively coupled plasma mass spectrometry (LA-ICP-MS; Materials and Methods) in three samples (80Z1, 90Z3, and 137Z1). The analytical sites are shown in fig. S8 (A to C). Given that the Atg and Ctl occur in the veins as micron-scale aggregates (fig. S5A), the trace element concentrations represent those of mixed Atg and Ctl. The Atg-Ctl veins are enriched in As and Sb and depleted in Ni and Co compared with the Lz in the matrix (Fig. 4 and fig. S9).

DISCUSSION

Subduction-related fluid infiltration during Atg-Ctl vein formation

The occurrence of Atg has only been reported at limited locations in the Oman ophiolite (*31*) where it is related to carbonated serpentinite and is inferred to have formed in preference to Ctl and lizardite due to high silica activity in aqueous fluids. The present study documented the occurrence of Atg in the crust-mantle transition zone. The cross-cutting relationships of Atg-Ctl vein and matrix indicate that the vein formation occurred after serpentinization of the matrix (i.e., the Lz + Brc mesh texture). The higher Ni concentration in the matrix with the mesh texture suggests that the first stage of serpentinization proceeded by replacing primary olivine (i.e., olivine has high Ni concentrations of ~3000 parts per million) (*40*). However, the lower Ni concentrations of the Atg-Ctl veins suggest that vein formation occurred after olivine serpentinization was complete.

In the Samail ophiolite, various fluid sources for serpentinization have been documented, such as circulating seawater at rigde (*27*, *28*), slab-derived fluids in the subduction zone (*22*), and ground and meteoric water (*28*). The bulk rock chemistry of serpentinized dunite recovered from a similar core sample showed a positive Eu anomaly (*37*), and in situ oxygen isotope data for

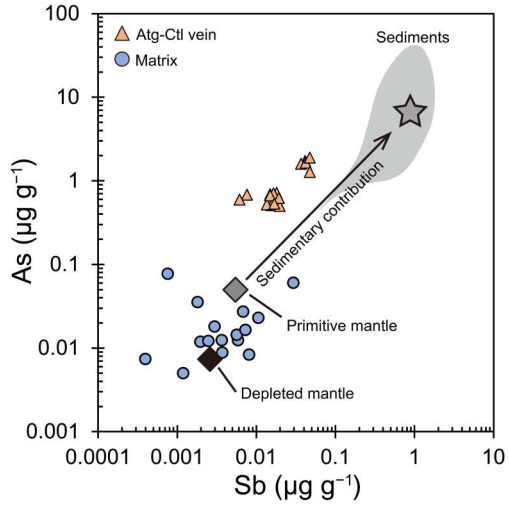

Fig. 4. Plot of As versus Sb concentrations for the Atg veins (orange triangles) and matrix (blue circles). The gray field represents oceanic sediments (the gray star is the average value for the oceanic sediments) (*72*). The gray and black symbols indicate the composition of the primitive (*73*) and depleted mantle (*74*), respectively.

serpentinites from the Samail Ophiolite indicate that temperature for serpentinization would be decreased from ~190° to ~30°C (*28*). These results suggest that the main serpentinization stage that formed the mesh texture occurred because of seafloor hydrothermal alteration. Our trace element data also support this hypothesis, because the Lz in the matrix has low As and Sb concentrations, similar to the depleted mantle (Fig. 4). In contrast, the enrichment of As and Sb in the Atg-Ctl vein (Fig. 4) suggests that the vein-forming fluids were partly sourced from subducted sediments (*41*, *42*). This is consistent with a recent study of serpentinite in the Samail ophiolite, which revealed that the serpentinite was affected by fluids derived from subducted sediments at temperatures of >400°C (*22*). These features suggest that Atg formation in the veins was due to fluid infiltration in a suprasubduction zone setting.

Conditions of Atg-Ctl vein and Brc-rich reaction zone formation

Ctl occurs between the Atg blades in the Atg-Ctl veins (fig. S5A) and in the wormholes and replacing mesh rims in the brucite-rich reaction zones (Fig. 3B). In addition, TEM observations of the reaction front of the Brc reaction zone show that Ctl occurs in the pore spaces between Brc crystals (Fig. 3D and fig. S7B). These occurrences suggest that formation of the Atg in the veins and reaction zones was followed by Ctl formation. Atg is considered as a high-temperature polytype of serpentine based on the natural occurrence of Atg (*43*, *44*). Although experimental studies of Atg formation from olivine are lacking at low-pressure conditions (<0.5 GPa), the mineral assemblage of Atg + Brc would be stable at 300° to 450°C and 0.1 to 0.5 GPa (*43*). Moreover, the infiltration of silica-rich fluid would have also induced Atg crystallization (*45*). Figure 5A is a stability diagram of temperature-silica activity at 200 MPa in the FeO-MgO-SiO_2-H_2O system, based on thermodynamic data for minerals (*46*) and the SUPCRTBL software (*47*). The phase diagram suggests that Atg is stable at higher temperatures and silica activities than Lz (Fig. 5A), which is consistent with natural occurrences of Atg at high temperatures (*44*) or high silica activities even at low temperatures (*31*, *45*). In the presence of Fe, the Lz stability field moves to higher temperatures, but the relationships with the other minerals remain similar. Ctl does not appear in the phase diagram (Fig. 5A), because it is metastable (*43*).

Previous studies of abyssal serpentinites have shown that Atg formation occurs by infiltration of silica-rich fluid based on the occurrences of Atg veins that are associated with talc (*45*). However, infiltration of silica-rich fluid is unlikely to explain the studied Atg-Ctl veins, because these have reaction zones that consist predominantly of Brc (Fig. 3A), which is only stable at low silica activities (i.e., several orders of magnitude lower than for talc; Fig. 5A) (*48*). Therefore, we consider that a relatively high-temperature fluid (300° to 450°C) (*43*) caused Atg to precipitate in fractures and form Brc-rich reaction zones.

Mass gains and losses of individual elements during the formation of the Brc-rich reaction zones via replacement of the matrix (Lz + Brc + Mag) were calculated using Gresens′ equation (Materials and Methods and Fig. 5B) (*49*). The whole-rock compositions of the Brc-rich reaction zone and matrix were obtained from the modal abundance and chemical compositions of individual minerals (tables S1 and S2). MgO, FeO, and H_2O show changes from gains to losses with decreasing volume factor (f_v = the ratio of the solid volume to the initial solid volume). In contrast, a substantial amount of SiO_2 (40 g of SiO_2 per 100 g of reacted rock) was removed from the host rocks regardless of the volume change (Fig. 5B), as the product mineral (Brc) does not contain SiO_2 (table S2).

To understand the chemical driving force for silica removal into the fractures, chemical potential gradients related to reaction zone formation were obtained on the basis of local equilibrium assumptions in the MgO-SiO_2-H_2O system for representative pressure-temperature (*P*-*T*) conditions. Figure 5 (C and D) shows the relationship between the Gibbs free energy of Atg, Lz, and Brc (per 48 moles of Mg) as a function of $aSiO_{2,aq}$ at 100° (Fig. 5C) and 350°C (Fig. 5D). The intersections of the Gibbs free energy in each diagram represent the Lz-Brc equilibrium conditions and Atg-Brc reactions

$$\underset{\text{lizardite}}{Mg_3Si_2O_5(OH)_4} + H_2O = 3\ \underset{\text{brucite}}{Mg(OH)_2} + 2\ SiO_{2(aq)} \quad (1)$$

and

$$\underset{\text{antigorite}}{Mg_{48}Si_{34}O_{85}(OH)_{62}} + 17\ H_2O = 48\ \underset{\text{brucite}}{Mg(OH)_2} + 34\ SiO_{2(aq)} \quad (2)$$

At 100°C, where Lz-Brc is stable, the silica activity ($aSiO_{2,aq}$) at Lz-Brc equilibrium ($\log[aSiO_{2,aq}] = -7.05$) is higher than at Atg-Brc equilibrium ($\log[aSiO_{2,aq}] = -7.00$) (Fig. 4C). In contrast, at 350°C, where Atg-Brc is stable, the silica activity ($aSiO_{2,aq}$) at the front of the Brc reaction zone (Lz-Brc equilibrium; $\log[aSiO_{2,aq}] = -4.02$) is higher than at the vein wall (Atg-Brc equilibrium; $\log[aSiO_{2,aq}] = -4.11$) (Fig. 4D). These results indicate that Atg-Brc is only stable when high-temperature fluids (i.e., 350°C) infiltrate. The difference in the chemical potential of silica between the host rock (Lz-Brc equilibrium) and Atg veins (Atg-Brc equilibrium) can cause the diffusion of aqueous silica, which formed the silica-depleted Brc reaction zone (Eq. 2). The topological

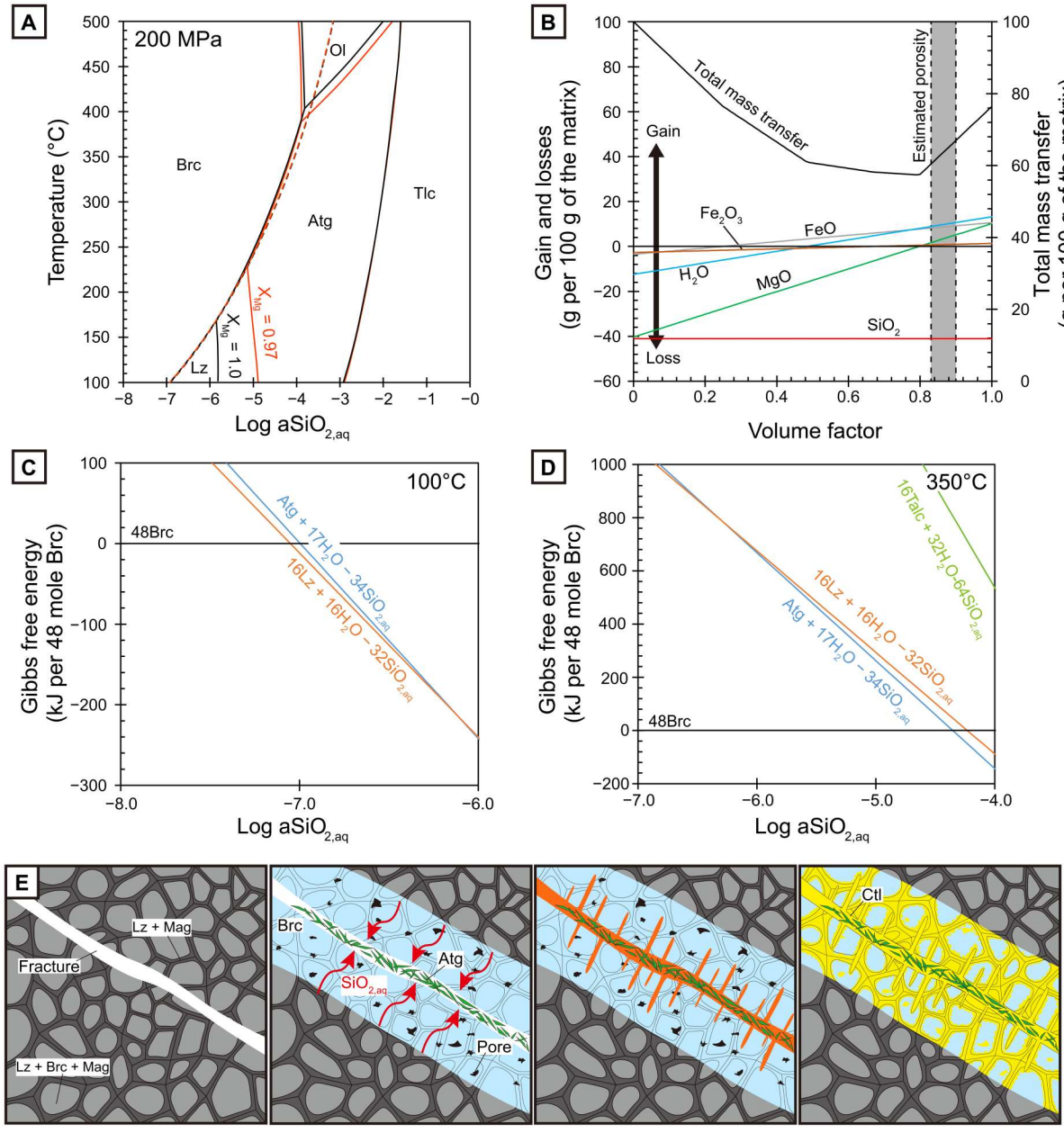

Fig. 5. Thermodynamic calculations on Atg and Brc-rich reaction zone. (**A**) $SiO_{2,aq}$ activity–temperature phase diagram of a X_{Mg}-fixed FeO-MgO-SiO_2-H_2O system at 200 MPa (black lines are for X_{Mg} = 1.0 and red lines are for X_{Mg} = 0.97). The dashed line shows the Lz-Brc equilibrium. (**B**) Gains and losses of species per unit volume of rock due to volume changes. The total mass transfer was calculated from the sum of the absolute values for each species. The gray area indicates the porosity in the reaction zone, as inferred from microstructural observations (see Materials and Methods). (**C** and **D**) Gibbs free energy (kJ per 48 mol Brc, X_{Mg} = 1.0) at different $aSiO_2$,aq values at (C) 100° and (D) 350°C. (**E**) Schematic model for reaction zone formation. The Brc reaction zone (blue) forms during Atg crystallization. Brc is rapidly dissolved by later fluid infiltration (orange) to form the wormhole texture. Brc is partly silicified along the mesh texture and converted to Ctl (yellow). Tlc, talc; Fo, forsterite.

relationship of the Gibbs free energy as a function of $aSiO_{2,aq}$ is robust, even if the uncertainties of the thermodynamic dataset for the serpentine minerals and Fe components are considered (Fig. 5A and Supplementary Text).

On the basis of microstructural observations and thermodynamic considerations, we propose the following scenario for the formation of the Atg-Ctl veins (Fig. 5E): (i) Dunite was completely serpentinized with mesh texture; (ii) a silica-poor fluid infiltrated along a fracture network, which resulted in Atg formation in the fractures and Brc reaction zones at temperatures of 300° to 450°C; and (iii) late-stage fluid infiltration dissolved Brc to form wormholes in the Brc reaction zones. After that, Ctl precipitated in the pore spaces of the Atg veins, and part of the Brc reaction zone was replaced by Ctl (Fig. 3B).

Analysis of TEM image (fig. S7A) indicate that the porosity of the host rock (Lz + Brc + Mag) is ~3%, which is consistent with

the porosity reported for serpentinized dunite in the Oman ophiolite (2.54 ± 1.51%) (*33*, *36*). In contrast, the porosity of the monomineralic Brc reaction zone that developed during Atg formation has been modified by the subsequent precipitation of Ctl (Figs. 3B and 5E). On the basis of the microstructural relationship between Brc and Ctl, we estimated that, during the formation of the Brc reaction zone, the porosity was 10 to 17% (see Materials and Methods). This value for the reaction zone is higher than that observed in the Lz + Brc + Mag matrix (~3%), as fluid-mediated mineral replacement reactions commonly generate porosity (up to ~30%) (*50*–*52*). The estimated porosity of 10 to 17% corresponds to f_v = 0.83 to 0.90, which is similar to the value obtained from minimizing the total mass transport (f_v = 0.80; Fig. 4B). Using f_v = 0.87 (i.e., the midvalue of the range 0.83 to 0.90), the reaction that resulted in the development of the Brc reaction zone is as follows

$$\underset{\text{lizardite}}{Mg_{2.91}Fe_{0.09}Si_2O_5(OH)_4} + 0.02\ \underset{\text{brucite 1}}{Mg_{0.85}Fe_{0.15}(OH)_2} + 0.40\ MgO + 0.35\ FeO + 1.76\ H_2O$$

$$= 3.78\ \underset{\text{brucite 2}}{Mg_{0.88}Fe_{0.12}(OH)_2} + 0.02\ Fe_2O_3 + 2\ SiO_2, aq \quad (3)$$

The formation of the Brc reaction zone required substantial mobilization of silica, whereas the other elements were relatively immobile during the formation of the reaction zone (Fig. 5B). This element mobilization contrasts with most reaction zones in metamorphic rocks, which is caused by the addition of elements from fluids [e.g., Cl (*19*) and CO_2 (*17*, *50*)]. Reaction zone formation induced by element removal has been reported for zones associated with quartz (*15*) and quartz + kyanite vein (*53*), caused by the low quartz solubility in an open crack (*15*). In the case of this study, the silica activity gradient was produced by the serpentine-Brc equilibria (Fig. 5D). The mobilization of silica and the pseudomorphic replacement of the serpentine mesh texture (Figs. 3B and 5E) suggest that the development of high porosity (10 to 17%) occurred before the precipitation of Ctl within reaction-induced pore spaces (Fig. 3D and fig. S7, A and B) or Brc was replaced by Ctl (Fig. 3B). The long-term existence of such pores along fractures may also affect the V_p/V_s anisotropy within the mantle wedge (*54*).

Velocity and duration of fluid drainage into a shallow mantle wedge

The drill core from Hole CM1A contains abundant vein networks in the mantle, crust-mantle transition zone, and lower crust (*33*). The Atg-Ctl veins occur mainly at depths of 160 to 180 m in Hole CM1A, where intense fault zones are commonly developed (Fig. 2A) (*33*), suggesting that these vein networks formed in association with faulting events. The occurrence of Atg-Ctl veins (Fig. 2) and their trace element compositions (Fig. 4 and fig. S9) indicate that infiltration of slab-derived fluids occurs in suprasubduction zones. The absence of banded internal textue (fig. S4, A and B) (*55*) in the Atg-Ctl veins suggests that each vein resulted from a single fluid flow event. In addition, it indicates that an open fracture persisted until mineral precipitation filled the fractue (*56*). This fluid could have been at higher temperatures (Atg-Brc equilibrium) than the host rock in which Lz-Brc was stable, although the precise temperature difference is not clear. Similar Atg vein networks have been reported in several ophiolites formed above subduction zones (*57*–*59*), suggesting that channelized fluid flow along fracture networks is common in suprasubduction zones. In general, while it seems that each individual vein was created by a single fluid flow event, the fact that the Atg-Ctl veins intersect each other (fig. S2) indicates that multiple fracturing and fluid flow events occurred to create the entire vein network.

The time-integrated fluid flux, duration, and fluid velocity along the fractures can be constrained by the presence of the Brc-rich reaction zones. The mass balance calculation and thermodynamic relationship suggest that silica was removed to form these reaction zones. Assuming that the silica concentration at the vein wall was zero, a minimum duration of reaction zone formation can be obtained. Alternatively, the fracture is filled with Atg. Hence, the silica concentration at Atg-Brc equilibrium is assumed to be the maximum silica concentration at the vein wall. Using a diffusion-controlled transport model for aqueous silica, we obtain a maximum duration of reaction zone formation (t_{RZ}) of 2.1×10^{-1} to 1.1×10^{1} years (Materials and Methods). The time scale is a maximum estimate, because increasing advective transport would enhance the migration rate of the reaction front. Although advection was neglected, this time scale is shorter than those estimated for vein formation in eclogites (~200 years) (*18*) and carbonation reactions related to ophiolite emplacement (~20 years) (*50*). Moreover, the estimated time scale for the Brc-rich reaction zone formation is much shorter than the duration from subduction initiation to emplacement of the Oman ophiolite (~20 Ma) (*29*). The fracture fluid flow velocity (v) was estimated from $v = Q_{TI}/(\phi_F t_{RZ})$, where ϕ_F is the fracture volume per unit volume (w_F [m]/1 [m]). The fracture aperture (w_F) was taken from the width of the Atg-Ctl veins (400 to 500 μm; fig. S6). The amount of silica released during formation of the Brc-rich reaction zones is higher than the amount used to precipitate Atg in the fractures (Materials and Methods). Therefore, the excess silica was transported by the fluid. Assuming that the silica concentration of the fluid in the fracture was zero, we obtained a fluid flow velocity, v, of 2.7×10^{-3} to 4.9×10^{-2} m s^{-1} (Materials and Methods). This velocity along the fractures in the mantle wedge is lower than that estimated for fluid flow related to EQs in the crust (~10^{-1} to 10^{1} m s^{-1}) (*60*, *61*) but similar to that estimated for tensile quartz veins in high-pressure metamorphic rocks in ancient subduction zones (~10^{-2} to 10^{-1} m s^{-1}) (*16*).

Subduction zone seismicity is closely linked to pore fluid pressure (*1*–*3*). The migration of epicenters and slip events above the subduction plate boundary has been observed in several subduction zones, such as Nankai and Cascadia (*10*, *11*, *62*–*64*). The epicenters move relatively slowly (~10^{-4} to 10^{-3} m s^{-1}) (*10*, *11*, *64*) as compared with the rupture velocity during major EQs (~10^{3} m s^{-1}) (*65*). The migration of epicenters has been observed at the depth of forearc mantle and is thought to represent fluid injection into the mantle wedge (*10*, *11*, *63*), which possibly lowers the pore fluid pressure at the subduction zone megathrust. We compared geophysical observations in the subduction zones with our estimate of the time scale and fluid flow velocity (Fig. 6). Our estimate of the time scale of reaction zone formation (2.1×10^{-1} to 1.1×10^{1} years) is close to the seismically observed time scale of fluid activity inferred from supraslab seismicity (~10^{-1} years) (*10*, *11*), silent EQs (10^{-1} to 10^{0} years) (*62*, *66*), and slow slip events (SSEs; 10^{-3} to 10^{-1} years) (*67*). In addition, the fluid velocity estimated for the Atg-Ctl veins (2.7×10^{-3} to 4.9×10^{-2} m s^{-1}) of the present

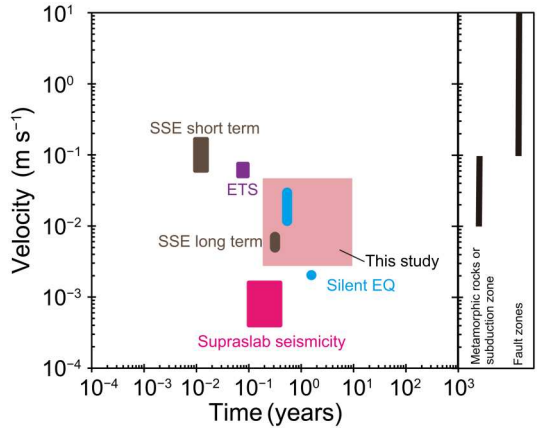

Fig. 6. Comparison of the characteristic velocities of propagation of seismic events and fluid flow estimated by petrological observations. The plot shows velocities and time scale of fluid flow for data obtained in this study (highlighted in red), as compared with the propagation velocities of slow slip events (SSEs) (*67*), episodic tremor and slip (ETS) (*64*), silent earthquake (EQ) (*62*, *66*), and supraslab seismicity (*10*, *11*). Fluid flow velocities in metamorphic rocks in ancient subduction zones (*16*) and fault zones (*60*, *61*) estimated on the basis of geological observation are shown on the right-hand side.

study is similar to the observed propagation velocities of episodic tremor and slip (ETS; ~10^{-1} m s^{-1}) (*12*, *64*), long-term SSE (~10^{-3} to 10^{-2} m s^{-1}) (*67*), and silent EQ (~10^{-3} to 10^{-2} m s^{-1}) (*62*, *66*). These values differ to the fluid velocity based on the permeability of intact serpentinite (~10^{-9} m s^{-1}) (*5*). The comparison of our geological evidence with geophysical observations suggests

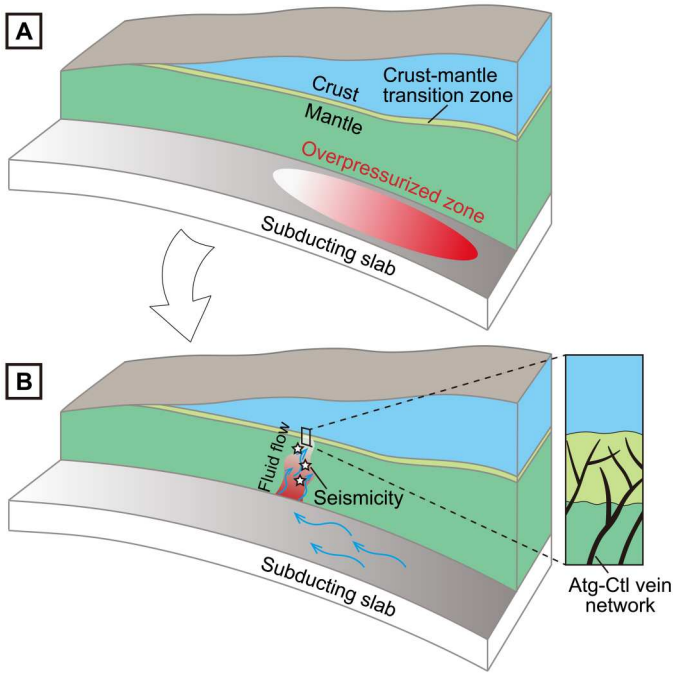

Fig. 7. Schematic model of subduction zone and a close-up view of the fracture zone. (**A**) Accumulation of fluids from subducting plate and buildup of pore fluid pressure. (**B**) Fluid flow through fracture network triggered by seismicity (white stars).

that, in contrast to the continuous nature of fluid supply from the subducting slab (Fig. 7A), some of the fluid drainage into the overlying plate occurs as transient pulses, possibly related to the migration of microseismicity (Fig. 7B). Such episodic fluid drainage causes rapid water-rock interactions within the mantle wedge. Moreover, we suggest that large, short-lived fluid fluxes through the mantle wedge can result in a decrease in pore fluid pressure, thereby influencing seismicity at a plate boundary.

MATERIALS AND METHODS

Analytical methods

The cores were scanned by x-ray micro-CT (Discovery CT750 HD, GE Medical Systems) onboard Chikyu. Three-dimensional images of 1.4 by 0.09 by 0.09 m with a voxel size of 0.176 by 0.176 by 0.625 mm were obtained with an excitation voltage of 140 kV and a current x-ray tube of 100 mA. The scanning rate was 20 mm/s (*33*). In addition, a selected area was scanned by high-resolution x-ray CT (ZEISS Xradia 520 Versa) at the High Energy Accelerator Research Organization, Japan. A three-dimensional image of 15 by 1 by 1 mm, with a voxel size of 2.98 by 2.98 by 2.98 μm, was obtained with an excitation voltage of 50 kV and an exposure time of 1.5 s.

An electron transparent foil across the reaction zone was prepared using a focused ion beam scanning electron microscopy (Thermo Fisher Scientific Helios G3 Nanolab, Utrecht University, the Netherlands). Subsequent analysis of the foil was carried out in a TEM (Thermo Fisher Scientific Talos F200X, Utrecht University) using both bright-field TEM imaging and scanning TEM imaging modes as well as energy-dispersive x-ray analysis.

Serpentine minerals were identified by Raman spectroscopy (HORIBA XploRA PLUS, Tohoku University, Japan) and a 532-nm green laser. The Raman spectra were collected over three scans, with an integration time of 10 s and a grating of 2400 grooves per mm. The chemical compositions of minerals were determined with an electron probe microanalyzer (EPMA; JEOL JXA-8200, Tohoku University, Japan), with an accelerating voltage of 15 kV, a beam current of 12 nA, and a beam diameter of 1 to 2 μm.

Trace element analysis of minerals was undertaken by LA-ICP-MS (ESI NWR193UC excimer LA system and Agilent 7700x quadrupole ICP-MS) at Akita University, Japan. The laser beam diameter was 140 μm for the analysis and 150 μm for the preablation. The other analytical conditions were: laser repetition rate = 10 Hz; He gas flow of 0.5 liter/min, with a He cup gas flow of 0.15 liter/min; Ar carrier gas flow of 0.68 liter/min, with an Ar dilution gas flow of 0.6 liter/min; laser ablation time = 70 s; and laser energy density = 8.0 J cm^{-2}. The NIST SRM 612 glass was used as the primary standard. The U.S. Geological Survey reference glasses BIR-1G and BHVO-2G were used as secondary standards to assess the data quality. The results are presented in table S4.

Mass balance calculations

Mass balance analysis was conducted to calculate the gains and losses of elements during alteration using Gresens′ equation (*49*) and the mineral modal abundances and chemical compositions (table S1). In Gresens′ equation, mass transfer is calculated by assuming a volumetric change in the difference between the bulk composition before and after the alteration. The bulk compositions of the reaction zone and host rock were determined from elemental maps (fig. S10) and mineral chemistry (table S1). Ctl was observed

along the reaction zone mesh rims (Fig. 3B), indicative of silicification of Brc (*48*) after the formation of the reaction zone (Fig. 5E). Therefore, it was assumed that the reaction zone consisted solely of Brc and Mag during its formation, and the Ctl volume was recalculated to be the Brc volume. The reaction zone and matrix contain fine-grained Mag (~1 μm), but it is difficult to identify these minerals in the EPMA maps. Therefore, the amount of the fine-grained Mag was determined from back-scattered electron (BSE) images (matrix = 2.0 area percent and reaction zone = 1.8 area percent; fig. S5, B and C). Hence, we assumed that the reaction zone consisted of 97.0 area percent of Brc [$Mg_{0.88}Fe_{0.12}(OH)_2$] and 3.0 area percent of Mag. The mineral mode in the matrix {97.5 area percent Lz [$Mg_{1.9}FeSi_{0.1}O_5(OH)_2$], 0.5 area percent Brc [$Mg_{0.85}Fe_{0.15}(OH)_2$], and 2.0 area percent Mag} was determined from BSE images and mineral phase mapping based on elemental maps of Si, Mg, Fe, and Cr using XMapTools (fig. S10) (*68*). Whole-rock compositions used in the mass balance calculation are provided in table S2. The mass balance was calculated using Gresens' equation (*49*)

$$f_v\left(\frac{\rho_{RZ}}{\rho_{\text{Wall rock}}}\right)c_n^{RZ} - c_n^{\text{Wall rock}} = x_n \quad (4)$$

where f_v is the volume factor and ρ_{RZ} and ρ_{Matrix} are the average density of the reaction zone and matrix, respectively, as follows

$$\rho_{\text{Matrix}} = \frac{A_{LZ}\rho_{LZ} + A_{Brc}\rho_{Brc} + A_{Mag}\rho_{Mag}}{A_{LZ} + A_{Brc} + A_{Mag}} \quad (5)$$

$$\rho_{RZ} = \frac{A_{Brc}\rho_{Brc} + A_{Mag}\rho_{Mag}}{A_{Brc} + A_{Mag}} \quad (6)$$

c_n^{RZ} and c_n^{Matrix} are the weight fractions of component n in the reaction zone and matrix, respectively, and x_n is the gain or loss for each component

$$c_n^{\text{Matrix}} = \frac{A_{LZ}\rho_{LZ}c_{LZ}^n + A_{Brc}\rho_{Brc}c_{Brc}^n + A_{Mag}\rho_{Mag}c_{Mag}^n}{\sum(A_{LZ}\rho_{LZ}c_{LZ}^n + A_{Brc}\rho_{Brc}c_{Brc}^n + A_{Mag}\rho_{Mag}c_{Mag}^n)} \quad (7)$$

$$c_n^{RZ} = \frac{(A_{Brc} - A_{\text{pore}})\rho_{Brc}c_{Brc}^n + A_{Mag}\rho_{Mag}c_{Mag}^n}{\sum(A_{Brc}\rho_{Brc}c_{Brc}^n + A_{Mag}\rho_{Mag}c_{Mag}^n)} \quad (8)$$

Measurement of the reaction zone widths from x-ray CT imaging

The x-ray micro-CT showed a high x-ray CT absorption in the reaction zone. The width of the reaction zone was determined by image processing using ImageJ software (*69*). A Euclidean distance map represents the distance to the nearest background pixel as a value for each pixel. Therefore, the pixel near the center of the reaction zone has a value of the width of the reaction zone. The center pixel was obtained by a thinning process, and the value of the pixel was used as the width of the reaction zone.

Estimation of porosity in the reaction zone

We estimated the porosity during the formation of the reaction zone. First, TEM observations of the Brc-rich reaction zone near the reaction front revealed that aggregates of acicular Ctl crystals occur in the pore spaces between Brc crystals (Fig. 3D and fig. S7B). This suggests that the Ctl in pore spaces was precipitated from the solution phase. Thus, the modal abundance of Ctl in the reaction zone could be regarded as the pore space that was present during the formation of the reaction zone and is accordingly estimated to be ~10%. Second, within the interiors of the Brc-rich reaction zones, the mesh-rim of Brc was preferentially replaced by Ctl (Fig. 3B), suggesting that Brc reacted with silica-rich fluid to form Ctl, as follows

$$\underset{\text{Brucite}}{3\,Mg(OH)_2} + 2SiO_{2,aq} \rightarrow \underset{\text{Serpentine}}{Mg_3(Si_2O_5)(OH)_4} + H_2O \quad (9)$$

This is a volume-increasing reaction with $V/V_0 = 1.44$. Using the V/V_0 value and the modal abundance of Ctl (55.3%), as well as the fact that the outline of the area of mesh texture is preserved within the reaction zone, we obtained a porosity of 17% for the Brc reaction zone before Ctl formation. On the basis of the porosity estimates for the two types of microstructures, the porosity range is 10 to 17%.

Silica activity at the front of the Brc reaction zone and vein wall

We calculate the fluid's silica activity at the reaction front and within the wall rock using equilibrium constants of i (K_i) for Lz, Atg, and Brc that can be written as follows

$$\underset{\text{lizardite}}{Mg_3Si_2O_5(OH)_4} + 6H^+ = 3Mg^{2+} + 2SiO_{2,aq} + 5H_2O$$

$$\log K_{LZ} = 2\log(a_{SiO_{2,aq}}) + 3\log\left[\frac{a_{Mg^{2+}}}{(a_{H^+})_2}\right] \quad (10)$$

$$\underset{\text{antigorite}}{Mg_{48}Si_{34}O_{85}(OH)_{62}} + 96H^+ = 48\,Mg^{2+} + 34SiO_{2,aq} + 79H_2O$$

$$\log K_{Atg} = 34\log(a_{SiO_{2,aq}}) + 48\log\left[\frac{a_{Mg^{2+}}}{(a_{H^+})^2}\right] \quad (11)$$

$$\underset{\text{brucite}}{Mg(OH)_2} = Mg^{2+} + 2OH^-$$

$$\log K_{Brc} = \log\left[\frac{a_{Mg^{2+}}}{(a_{H^+})^2}\right] \quad (12)$$

Assuming equilibrium between Brc and Lz, the silica activity at the reaction front can be obtained by combining Eqs. 10 and 12.

$$\log(a_{SiO_{2,aq}}) = \frac{1}{2}(\log K_{LZ} - 3\log K_{Brc}) \quad (13)$$

Assuming equilibrium between Brc and Atg, the silica activity at the reaction front can be obtained by combining Eqs. 11 and 12

$$\log(a_{SiO_{2,aq}}) = \frac{1}{34}(\log K_{Atg} - 48\log K_{Brc}) \quad (14)$$

Time scales of Atg-Ctl vein formation

The sharp reaction front of the Brc reaction zone (Fig. 3, A and D) suggests that the migration of the front is rate limited by diffusive transport rather than surface reaction (*70*). The diffusive flux of silica ($Q_{SiO_{2,aq}}$ [mol m^{-2} s^{-1}]) from the reaction zone is given by

$$Q_{SiO_{2,aq}} = D_{SiO_{2,aq}} \varphi_{RZ} \frac{dC_{SiO_{2,aq}}}{dx} \approx D_{SiO_{2,aq}} \varphi_{RZ} \frac{(C^{\text{Reaction front}}_{SiO_{2,aq}} - C^{\text{Vein wall}}_{SiO_{2,aq}})}{x} \rho_w \quad (15)$$

where $D_{SiO_{2,aq}}$ (m^2 s^{-1}) is the diffusion coefficient of silica in water; $C^{\text{Reaction front}}_{SiO_{2,aq}}$ and $C^{\text{Vein wall}}_{SiO_{2,aq}}$ [mol $kg^{-1}_{(water)}$] are the silica concentrations at the reaction front and vein wall, respectively. ρ_{RZ} and ρ_w are the densities of the reaction zone and water, respectively; x is the distance from the reaction front to the fluid; and ϕ_{RZ} is the porosity of the reaction zone. The migration rate of the reaction zone is given by

$$\frac{dx}{dt} = \frac{Q_{SiO_{2,aq}}}{n_{RZ}} \quad (16)$$

where t (s) is the time and n_{RZ} [mol $m^{-3}_{(RZ)}$] is the number of moles of $SiO_{2,aq}$ that are produced to form a reaction zone with a volume of 1 m^3. Combining Eqs. 15 and 16, the time scale to form a reaction zone with a width of w_{RZ} can be written as follows

$$t_{RZ} = \frac{1}{2} \frac{n_{RZ}}{D_{SiO_{2,aq}} \varphi_{RZ} (C^{\text{Reaction front}}_{SiO_{2,aq}} - C^{\text{Vein wall}}_{SiO_{2,aq}}) \rho_w} w_{RZ^2} \quad (17)$$

$D_{SiO2,aq}$ was set to 2.5×10^{-8} m^2 s^{-1}, considering that the diffusivity for aqueous ionic species at 350°C and 100 to 300 MPa varies from 1×10^{-8} to 5×10^{-8} m^2 s^{-1} (*71*). We set w_{RZ} to the observed width of the Brc-rich reaction zones (0.5 to 1.3 mm; Fig. 3E) and ϕ_{RZ} to 10 to 17%. All parameters used in the calculation are shown in table S3.

Estimation of the fluid flow velocity

To determine the fluid flow velocity, we considered a unit volume (1 by 1 by 1 m) of host rock with a single fracture and reaction zones on both sides of the fracture. The total amount of fluid flow that passes across an area of the fracture [Q_{TI}; $m^3_{(water)}$] is approximately as follows

$$Q_{TI} \approx \frac{\xi_{RZ} n_{RZ} - \xi_{vein} n_{Atg}}{C^{\text{Vein wall}}_{SiO_{2,aq}} \rho_w} \quad (18)$$

where ξ_{RZ} (= $2w_{RZ}$ per unit length) and ξ_F (= w_F per unit length) are the volume fractions of the reaction zone and fracture. The numerator represents the amount of silica that must be transported by the fluid (7.7 to 37.3 moles). The average fluid flow velocity v (m s^{-1}) is given by the cross-sectional area of the fracture ($A_F = w_F \cdot$ unit length) and duration of the fluid flow (t_{RZ}), $v = Q_{TI}/(A_F t_{RZ})$.

Supplementary Materials

This PDF file includes:

Supplementary Text
Figs. S1 to S10
Tables S1 to S6

REFERENCES AND NOTES

1. D. M. Saffer, H. J. Tobin, Hydrogeology and mechanics of subduction zone forearcs: Fluid flow and pore pressure. *Annu. Rev. Earth Planet. Sci.* **39**, 157–186 (2011).
2. P. Audet, M. G. Bostock, N. I. Christensen, S. M. Peacock, Seismic evidence for overpressured subducted oceanic crust and megathrust fault sealing. *Nature* **457**, 76–78 (2009).
3. S. Kodaira, T. Iidaka, A. Kato, J.-O. Park, T. Iwasaki, Y. Kaneda, High pore fluid pressure may cause silent slip in the nankai trough. *Science* **304**, 1295–1298 (2004).
4. B. R. Hacker, S. M. Peacock, G. A. Abers, S. D. Holloway, Subduction factory 2. Are intermediate-depth earthquakes in subducting slabs linked to metamorphic dehydration reactions? *J. Geophys. Res. Solid Earth* **108**, e2001JB001129 (2003).
5. S. Kawano, I. Katayama, K. Okazaki, Permeability anisotropy of serpentinite and fluid pathways in a subduction zone. *Geology* **39**, 939–942 (2011).
6. A. Yamaguchi, K. Ujiie, S. Nakai, G. Kimura, Sources and physicochemical characteristics of fluids along a subduction-zone megathrust: A geochemical approach using syn-tectonic mineral veins in the Mugi mélange, Shimanto accretionary complex. *Geochem. Geophys. Geosystems* **13**, e2012GC004137 (2012).
7. R. D. Hyndman, S. M. Peacock, Serpentinization of the forearc mantle. *Earth Planet. Sci. Lett.* **212**, 417–432 (2003).
8. S. A. Peacock, Fluid processes in subduction zones. *Science* **248**, 329–337 (1990).
9. S. Husen, E. Kissling, Postseismic fluid flow after the large subduction earthquake of Antofagasta Chile. *Geology* **29**, 847–850 (2001).
10. J. Nakajima, N. Uchida, Repeated drainage from megathrusts during episodic slow slip. *Nat. Geosci.* **11**, 351–356 (2018).
11. S. E. J. Nippress, A. Rietbrock, Seismogenic zone high permeability in the Central Andes inferred from relocations of micro-earthquakes. *Earth Planet. Sci. Lett.* **263**, 235–245 (2007).
12. K. Obara, Nonvolcanic deep tremor associated with subduction in Southwest Japan. *Science* **296**, 1679–1681 (2002).
13. S. Aretusini, F. Meneghini, E. Spagnuolo, C. W. Harbord, G. di Toro, Fluid pressurisation and earthquake propagation in the Hikurangi subduction zone. *Nat. Commun.* **12**, 2481 (2021).
14. R. H. Sibson, Stress switching in subduction forearcs: Implications for overpressure containment and strength cycling on megathrusts. *Tectonophysics* **600**, 142–152 (2013).
15. D. M. Fisher, S. L. Brantley, The role of silica redistribution in the evolution of slip instabilities along subduction interfaces: Constraints from the Kodiak accretionary complex, Alaska. *J. Struct. Geol.* **69**, 395–414 (2014).
16. A. Okamoto, N. Tsuchiya, Velocity of vertical fluid ascent within vein-forming fractures. *Geology* **37**, 563–566 (2009).
17. A. Okamoto, R. Oyanagi, K. Yoshida, M. Uno, H. Shimizu, M. Satish-Kumar, Rupture of wet mantle wedge by self-promoting carbonation. *Commun. Earth Environ.* **2**, 151 (2021).
18. T. John, N. Gussone, Y. Y. Podladchikov, G. E. Bebout, R. Dohmen, R. Halama, R. Klemd, T. Magna, H. M. Seitz, Volcanic arcs fed by rapid pulsed fluid flow through subducting slabs. *Nat. Geosci.* **5**, 489–492 (2012).
19. D. Mindaleva, M. Uno, F. Higashino, T. Nagaya, A. Okamoto, N. Tsuchiya, Rapid fluid infiltration and permeability enhancement during middle–lower crustal fracturing: Evidence from amphibolite–granulite-facies fluid–rock reaction zones, Sør Rondane Mountains, East Antarctica. *Lithos* **372–373**, 105521 (2020).
20. R. J. Cowan, M. P. Searle, D. J. Waters, Structure of the metamorphic sole to the Oman ophiolite, Sumeini Window and Wadi Tayyin: Implications for ophiolite obduction processes. *Geol. Soc. Spec. Publ.* **392**, 155–175 (2014).
21. M. Yoshikawa, M. Python, A. Tamura, S. Arai, E. Takazawa, T. Shibata, A. Ueda, T. Sato, Melt extraction and metasomatism recorded in basal peridotites above the metamorphic sole of the northern Fizh massif, Oman ophiolite. *Tectonophysics* **650**, 53–64 (2015).
22. J. C. Obeso, P. B. Kelemen, J. M. Leong, M. D. Menzel, C. E. Manning, M. Godard, Y. Cai, L. Bolge, Deep sourced fluids for peridotite carbonation in the shallow mantle wedge of a fossil subduction zone: Sr and C isotope profiles of OmanDP hole BT1B. *J. Geophys. Res. Solid Earth* **127**, e2021JB022704 (2022).
23. C. A. Hopson, R. G. Coleman, R. T. Gregory, J. S. Pallister, E. H. Bailey, Geologic section through the Samail Ophiolite and associated rocks along a Muscat-Ibra Transect, southeastern Oman mountains. *J. Geophys. Res. Solid Earth* **86**, 2527–2544 (1981).
24. M. Rioux, S. Bowring, P. Kelemen, S. Gordon, F. Dudás, R. Miller, Rapid crustal accretion and magma assimilation in the Oman-U.A.E. ophiolite: High precision U-Pb zircon geochronology of the gabbroic crust. *J. Geophys. Res. Solid Earth* **117**, 7201 (2012).
25. A. Nicolas, F. Bouldier, B. Ildefonse, E. Ball, Accretion of Oman and United Arab Emirates ophiolite–Discussion of a new structural map. *Mar. Geophys. Res.* **21**, 147–180 (2000).
26. C. E. Manning, C. J. MacLeod, P. E. Weston, "Lower-crustal cracking front at fast-spreading ridges: Evidence from the East Pacific Rise and the Oman Ophiolite" in *Ophiolites and oceanic crust: New insights from field studies and the Ocean Drilling Program* (Geological Society of America, 2000);https://pubs.geoscienceworld.org/books/book/501/chapter/3800676.

27. C. Aupart, L. Morales, M. Godard, B. Jamtveit, Seismic faults triggered early stage serpentinization of peridotites from the Samail Ophiolite, Oman. *Earth Planet Sci. Lett.* **574**, 117137 (2021).
28. M. R. Scicchitano, M. J. Spicuzza, E. T. Ellison, D. Tuschel, A. S. Templeton, J. W. Valley, In situ oxygen isotope determination in serpentine minerals by SIMS: Addressing matrix effects and providing new insights on serpentinisation at Hole BA1B (Samail Ophiolite, Oman). *Geostand. Geoanal. Res.* **45**, 161–187 (2021).
29. B. R. Hacker, J. L. Mosenfelder, E. Gnos, Rapid emplacement of the Oman ophiolite: Thermal and geochronologic constraints. *Tectonics* **15**, 1230–1247 (1996).
30. M. P. Searle, Structural geometry, style and timing of deformation in the Hawasina Window, Al Jabal al Akhdar and Saih Hatat culminations, Oman mountains. *GeoArabia* **12**, 99–130 (2007).
31. E. S. Falk, P. B. Kelemen, Geochemistry and petrology of listvenite in the Samail Ophiolite, Sultanate of Oman: Complete carbonation of peridotite during ophiolite emplacement. *Geochim. Cosmochim. Acta* **160**, 70–90 (2015).
32. P. B. Kelemen, J. Matter, E. E. Streit, J. F. Rudge, W. B. Curry, J. Blusztajn, Rates and mechanisms of mineral carbonation in peridotite: Natural processes and recipes for enhanced, in situ CO_2 capture and storage. *Annu. Rev. Earth Planet. Sci.* **39**, 545–576 (2011).
33. P. B. Kelemen, J. M. Matter, D. A. H. Teagle, J. A. Coggon, the Oman Drilling Project Science Team, in *Proceedings of the Oman Drilling Project* (International Ocean Discovery Program, 2020), vol. phase 1 and 2.
34. C. Zhang, J. Koepke, P. E. Wolff, I. Horn, D. Garbe-Schönberg, J. Berndt, Multi-stage hydrothermal veins in layered gabbro of the Oman ophiolite: Implications for focused fluid circulation in the lower oceanic crust. *J. Geophys. Res. Solid Earth* **126**, e2021JB022349 (2021).
35. K. Yoshida, A. Okamoto, H. Shimizu, R. Oyanagi, N. Tsuchiya, Fluid infiltration through oceanic lower crust in response to reaction-induced fracturing: Insights from serpentinized troctolite and numerical models. *J. Geophys. Res. Solid Earth* **125**, e2020JB020268 (2020).
36. I. Katayama, N. Abe, K. Hatakeyama, Y. Akamatsu, K. Okazaki, O. I. Ulven, G. Hong, W. Zhu, B. Cordonnier, K. Michibayashi, M. Godard, P. Kelemen, Permeability profiles across the crust-mantle sections in the oman drilling project inferred from dry and wet resistivity data. *J. Geophys. Res. Solid Earth* **125**, e2019JB018698 (2020).
37. F. Kourim, M. Rospabé, N. Dygert, S. Chatterjee, E. Takazawa, K. -L. Wang, M. Godard, M. Benoit, M. Giampouras, K. Ishii, D. A. -H. Teagle, M. -J. Cooper, P. Kelemen, Geochemical characterization of the oman crust-mantle transition zone, OmanDP Holes CM1A and CM2B. *J. Geophys. Res. Solid Earth* **127**, e2021JB022694 (2022).
38. P. Szymczak, A. J. C. Ladd, Wormhole formation in dissolving fractures. *J. Geophys. Res. Solid Earth* **114**, B06203 (2009).
39. O. Devauchelle, P. Szymczak, M. Pecelerowicz, Y. Cohen, H. J. Seybold, D. H. Rothman, Laplacian networks: Growth, local symmetry, and shape optimization. *Phys. Rev. E* **95**, 033113 (2017).
40. H. Sato, Nickel content of basaltic magmas: Identification of primary magmas and a measure of the degree of olivine fractionation. *Lithos* **10**, 113–120 (1977).
41. F. Deschamps, S. Guillot, M. Godard, M. Andreani, K. Hattori, Serpentinites act as sponges for fluid-mobile elements in abyssal and subduction zone environments. *Terra Nova* **23**, 171–178 (2011).
42. H. Hattori, S. Guillot, Volcanic fronts form as a consequence of serpentinite dehydration in the forearc mantle wedge. *Geology* **6**, 525–528 (2003).
43. B. W. Evans, The serpentinite multisystem revisited: Chrysotile is metastable. *Int. Geol. Rev.* **46**, 479–506 (2004).
44. S. Schwartz, S. Guillot, B. Reynard, R. Lafay, B. Debret, C. Nicollet, P. Lanari, A. L. Auzende, Pressure-temperature estimates of the lizardite/antigorite transition in high pressure serpentinites. *Lithos* **178**, 197–210 (2013).
45. S. Rouméjon, M. Andreani, G. L. Früh-Green, Antigorite crystallization during oceanic retrograde serpentinization of abyssal peridotites. *Contrib. Mineral. Petrol.* **174**, 60 (2019).
46. T. J. B. Holland, R. Powell, An improved and extended internally consistent thermodynamic dataset for phases of petrological interest, involving a new equation of state for solids. *J. Metam. Geol.* **29**, 333–383 (2011).
47. K. Zimmer, Y. Zhang, P. Lu, Y. Chen, G. Zhang, M. Dalkilic, C. Zhu, SUPCRTBL: A revised and extended thermodynamic dataset and software package of SUPCRT92. *Comput. Geosci.* **90**, 97–111 (2016).
48. B. M. Tutolo, A. J. Luhmann, N. J. Tosca, W. E. Seyfried, Serpentinization as a reactive transport process: The brucite silicification reaction. *Earth Planet. Sci. Lett.* **484**, 385–395 (2018).
49. R. L. Gresens, Composition-volume relationships of metasomatism. *Chem. Geol.* **2**, 47–65 (1967).
50. A. Beinlich, T. John, J. C. Vrijmoed, M. Tominaga, T. Magna, Y. Y. Podladchikov, Instantaneous rock transformations in the deep crust driven by reactive fluid flow. *Nat. Geosci.* **13**, 307–311 (2020).
51. N. Beaudoin, A. Hamilton, D. Koehn, Z. K. Shipton, U. Kelka, Reaction-induced porosity fingering: Replacement dynamic and porosity evolution in the KBr-KCl system. *Geochim. Cosmochim. Acta* **232**, 163–180 (2018).
52. O. Plümper, A. Botan, C. Los, Y. Liu, A. Malthe-Sørenssen, B. Jamtveit, Fluid-driven metamorphism of the continental crust governed by nanoscale fluid flow. *Nat. Geosci.* **10**, 685–690 (2017).
53. J. J. Ague, Extreme channelization of fluid and the problem of element mobility during Barrovian metamorphism. *Am. Mineral.* **96**, 333–352 (2011).
54. G. T. Kuster, M. N. Toksöz, Velocity and attenuation of seismic waves in two-phase media: Part I. Theoretical formulations. *Geophysics* **39**, 587–606 (1974).
55. M. S. Tarling, S. A. F. Smith, J. S. Rooney, C. Viti, K. C. Gordon, A common type of mineralogical banding in serpentine crack-seal veins. *Earth Planet Sci. Lett.* **564**, 116930 (2021).
56. D. M. Fisher, J. N. Hooker, A. J. Smye, T. W. Chen, Insights from the geological record of deformation along the subduction interface at depths of seismogenesis. *Geosphere* **17**, 1686–1703 (2021).
57. O. Dandar, A. Okamoto, M. Uno, N. Tsuchiya, Redistribution of magnetite during multistage serpentinization: Evidence from the Taishir Massif, Khantaishir ophiolite, western Mongolia. *J. Mineral. Petrol. Sci.* **116**, 176–181 (2021).
58. E. J. Carter, B. O'Driscoll, R. Burgess, P. L. Clay, Multi-stage fluid infiltration and metasomatism in supra-subduction zone mantle: Evidence from halogens and noble gases in the Leka Ophiolite Complex, Norway. *Geochim. Cosmochim. Acta* **307**, 258–280 (2021).
59. M. Ulrich, M. Muñoz, P. Boulvais, M. Cathelineau, D. Cluzel, S. Guillot, C. Picard, Serpentinization of New Caledonia peridotites: From depth to (sub-)surface. *Contrib. Mineral. Petrol.* **175**, 1–25 (2020).
60. N. H. S. Oliver, M. J. Rubenach, B. Fu, T. Baker, T. G. Blenkinsop, J. S. Cleverley, L. J. Marshall, P. J. Ridd, Granite-related overpressure and volatile release in the mid crust: Fluidized breccias from the Cloncurry district, Australia. *Geofluids* **6**, 346–358 (2006).
61. S. F. Cox, S. M. Munroe, Breccia formation by particle fluidization in fault zones: Implications for transitory, rupture-controlled fluid flow regimes in hydrothermal systems. *Am. J. Sci.* **316**, 241–278 (2016).
62. V. Kostoglodov, S. K. Singh, J. A. Santiago, S. I. Franco, K. M. Larson, A. R. Lowry, R. Bilham, A large silent earthquake in the Guerrero seismic gap, Mexico. *Geophys. Res. Lett.* **30**, e2003GL017219 (2003).
63. F. Halpaap, S. Rondenay, A. Perrin, S. Goes, L. Ottemöller, H. Austrheim, R. Shaw, T. Eeken, Earthquakes track subduction fluids from slab source to mantle wedge sink 5, eaav7369 (2019).
64. H. Dragert, K. Wang, G. Rogers, Geodetic and seismic signatures of episodic tremor and slip in the northern Cascadia subduction zone. 56, 1143–1150 (2004).
65. C. D. Rowe, W. A. Griffith, Do faults preserve a record of seismic slip: A second opinion. *J. Struct. Geol.* **78**, 1–26 (2015).
66. S. Ozawa, M. Murakami, M. Kaidzu, T. Tada, T. Sagiya, Y. Hatanaka, H. Yarai, T. Nishimura, Detection and monitoring of ongoing aseismic slip in the Tokai region, central Japan. *Science* **298**, 1009–1012 (2002).
67. H. Hirose, K. Obara, Repeating short-and long-term slow slip events with deep tremor activity around the Bungo channel region, southwest Japan. *Earth Planet Space* **57**, 961–972 (2005).
68. P. Lanari, O. Vidal, V. de Andrade, B. Dubacq, E. Lewin, E. G. Grosch, S. Schwartz, XMapTools: A MATLAB©-based program for electron microprobe X-ray image processing and geothermobarometry. *Comput. Geosci.* **62**, 227–240 (2014).
69. C. A. Schneider, W. S. Rasband, K. W. Eliceiri, NIH Image to ImageJ: 25 years of image analysis. *Nat. Methods* **9**, 671–675 (2012).
70. P. C. Lichtner, The quasi-stationary state approximation to coupled mass transport and fluid-rock interaction in a porous medium. *Geochim. Cosmochim. Acta* **52**, 143–165 (1988).
71. E. H. Oelkers, H. C. Helgeson, Calculation of the thermodynamic and transport properties of aqueous species at high pressures and temperatures: Aqueous tracer diffusion coefficients of ions to 1000°C and 5 kb. *Geochim. Cosmochim. Acta* **52**, 63–85 (1988).
72. T. Plank, J. N. Ludden, 8. Geochemistry of sediments in the argo abyssal plain at site 765: A continental margin reference section for sediment recycling in subduction zones. *Proc. Ocean Drill. Prog. Sci. Results* **123**, 167–189 (1992).
73. W. F. McDonough, S. S. Sun, The composition of the Earth. *Chem. Geol.* **120**, 223–253 (1995).
74. V. J. M. Salters, A. Stracke, Composition of the depleted mantle. *Geochem. Geophys. Geosystems* **5**, Q05B07 (2004).

Acknowledgments: This research used samples and data provided by the Oman Drilling Project (OmanDP). We thank all members of the OmanDP for the sample collection, descriptions, and x-ray CT scanning onboard Chikyu. We also thank Y. Niwa and T. Ishii for conducting the x-ray CT imaging; A. Chogani for helping with the TEM sample preparation; and M. Uno, L. Eberhard, and F. Klein for valuable discussions. We thank P. B. Kelemen for

commenting on an earlier version of the manuscript. **Funding:** This work was supported by JSPS KAKENHI grants JP21J20281, JP17H02981, JP18KK0376, JP21H01189, JP22H04932, JP22H05295, and JP22H05109; European Research Council (ERC) starting grant (nanoEARTH; 852069); and International Joint Graduate Program in Earth and Environmental Sciences, Tohoku University (GP-EES). **Author contributions:** Conceptualization: A.O., R.O., and K.Y. Methodology: R.O. and K.Y. Investigation: A.O., R.O., K.Y., M.K., O.P., and M.F. Visualization: K.Y. Supervision: A.O. Writing (original draft): K.Y. Writing (review and editing): A.O., R.O., M.K., O.P., and M.F. **Competing interests:** The authors declare that they have no competing interests. **Data and materials availability:** All data needed to evaluate the conclusions in the paper are present in the paper, the Supplementary Materials, and open-access repository. Onboard XCT data used in this study are archived on the OmanDP website (https://doi.org/10.14379/OmanDP.proc.2020). Animation of XCT in Fig. 3C and chemical analysis data in tables S1 and S4 to S6 are available at the open-access figshare repository (https://doi.org/10.6084/m9.figshare.19450313).

Submitted 31 August 2022
Accepted 7 March 2023
Published 5 April 2023
10.1126/sciadv.ade6674

ScienceAdvances

Geological records of transient fluid drainage into the shallow mantle wedge

Kazuki Yoshida, Ryosuke Oyanagi, Masao Kimura, Oliver Plmper, Mayuko Fukuyama, and Atsushi Okamoto

Sci. Adv., **9** (14), eade6674.
DOI: 10.1126/sciadv.ade6674

Science Advances (ISSN) is published by the American Association for the Advancement of Science. 1200 New York Avenue NW, Washington, DC 20005. The title *Science Advances* is a registered trademark of AAAS.